PHYSICAL REVIEW C VOLUME 20, NUMBER 5 NOVEMBER 1979

Optical model analysis for $^{16}O + ^{208}Pb$: Evidence for dynamic shape or density changes

Hugues Delagrange*
Department of Chemistry, State University of New York at Stony Brook, Stony Brook, New York 11794

Louis C. Vaz
Department of Chemistry, State University of New York at Stony Brook, Stony Brook, New York 11794
and Departmento de Fisica Nuclear, I.F.U.F.R.J., Cidade Universitaria, Ilha do Fundao, Rio de Janeiro, R. J. Brasil 20.000

John M. Alexander
Department of Chemistry, State University of New York at Stony Brook, Stony Brook, New York 11794
(Received 20 April 1979)

For the reaction $^{16}O + ^{208}Pb$, experimental data are available for cross sections for complete fusion and all reactions from 80–102 MeV and for elastic scattering from 80 to 313 MeV. Most of these data can be adequately described by an energy-independent spherical optical potential with the proximity formulation for the real part and a Woods-Saxon form for the imaginary part. Three parameters have been varied, radius and surface width in the proximity potential and radius in the imaginary potential. The sum of the equivalent sharp radii of the interacting nuclei must be enlarged significantly in order to fit the fusion and scattering data. As a consequence, the sum of the "best fit central radii" for ^{16}O and ^{208}Pb is ≈ 0.8 fm larger than the sum of the independently measured radii. If the proximity formulation is correct this implies dynamical shape or density adjustments during the collision.

[NUCLEAR REACTIONS Optical model analysis for the reaction system $^{16}O + ^{208}Pb$: fusion and reaction cross sections (80–102 MeV) and elastic scattering cross sections (80–313 MeV).]

I. INTRODUCTION

In a series of papers we have discussed the combination of constraints imposed on a conservative potential (between complex nuclei) by experimental data on reaction, fusion, and scattering cross sections.[1-5] We have proposed the following sequence of steps[3] to delimit the ion-ion potential: (1) From the complete fusion cross sections (σ_{cf}) at low energies adjust the maximum in the real s-wave barrier[5] (Coulomb plus nuclear potential). (2) From the quarter points for elastic scattering ($\theta_{1/4}$) adjust the tail of the nuclear potential[4] (with the barrier height fixed). (3) From the reaction cross sections and the detailed shapes of the elastic scattering data adjust the imaginary potential and refine the shape of the real potential.[3] We have applied the first step above to excitation functions for complete fusion for 48 reaction systems. Also, for the one system $^{16}O + ^{208}Pb$ we applied the first two steps and made a start on the third.[3] In this paper we return to the same reaction system and make a more detailed study with higher standards for the fits to experimental data on elastic scattering over a wide energy range (80–313 MeV).

For the real potential we use the proximity potential formulation of Blocki *et al.*[6] Several studies have demonstrated that the trends of this potential are in qualitative agreement with data for heavy ion collisions.[6-11] In addition, however, certain quantitative difficulties have been pointed out.[3,5,12] Our calculations are made largely in the context of the quantum mechanical optical model with an imaginary potential of the Woods-Saxon form. This imaginary potential provides the absorption or reaction processes and is our only simulator of frictional effects.[3] Birkelund *et al.* have made calculations of fusion cross sections with explicit comparisons of a "friction-free" model to a model including one-body friction.[10] At near-barrier energies their calculated results with the two models are very similar. In both their calculations and ours, the criterion for complete fusion is the traversal of the real potential maximum.[3-5,8-10] After such traversal the collision partners are assumed to fuse; there is no low-l cutoff in these models at present.[13]

We have sought to fit the experimental data with three free parameters, the equivalent sharp radius (R) and surface width (b) of the real potential and the radius (R_I) of the imaginary potential (depth and diffuseness of the imaginary potential have been held constant).[3] In the optical model calculations with the unadjusted proximity potential, we have not been able to fit most data. After small adjustments to the parameters, R and b in the real potential, we have obtained very good fits to the data, with significant deviations only at the lowest

energies. These adjustments in the real potential are very significant and important[3,5]; for fixed distance between the charge centers, the real nuclear potential must be almost doubled as compared to the parametrization suggested by Blocki *et al.*[6] This strengthening of the real potential has been achieved by enlarging the radii of the collision partners. The "best fit" value of the sum of equivalent sharp radii for ^{16}O and ^{208}Pb is ≈0.8 fm larger than that inferred from electron and proton scattering. The imaginary potential we use is weaker than the real one for the sensitive regions (i.e., $11 < r < 13$ fm or $1 < \zeta < 3.5$), but nevertheless provides strong absorption for the more penetrating trajectories. At higher energies most features of the elastic scattering are dominated by the real potential.[4] At lower energies the elastic scattering is very sensitive to the imaginary potential.[3] The total reaction cross section is clearly sensitive to the imaginary potential at all energies, but the sensitivity is especially great near the barrier.[3]

II. THE OPTICAL MODEL POTENTIAL, ITS PARAMETERS, AND THE MECHANICS OF THE CALCULATIONS

The optical model potential we use has the standard form defined as follows:

$$V(r) = V_c(r) + V_N(r) - iW_I(r), \tag{1}$$

where[3,4]

$$\begin{aligned} V_c(r) &= Z_t Z_p e^2/r, \quad r \geq R_c \\ &= (Z_t Z_p e^2/2R_c)(3 - r^2/R_c^2), \quad r \leq R_c \\ R_c &= 1.3(A_t^{1/3} + A_p^{1/3}). \end{aligned} \tag{2}$$

V_N is the nuclear part for which we use the idealization of frozen nuclear spheres. This potential is controlled by three parameters[6]; b, the surface width; R, the equivalent sharp radius of the matter distribution; and γ, the surface energy coefficient. Recommended values of these parameters[6] are as follows with our additions of Δb, and ΔR[3,5]:

$$b = 1.0 + \Delta b \text{ (fm)}, \tag{3}$$

$$R = 1.28A^{1/3} - 0.76 + 0.8A^{-1/3} + \Delta R \text{ (fm)}, \tag{4}$$

$$\gamma = 0.9517\{1 - 1.7826[(N - Z)/A]^2\} \text{ (MeV/fm}^2\text{)}, \tag{5}$$

where N, Z, and A refer to the combined system of the two separate interacting nuclei.

In the proximity force representation, the potential V_N is defined by

$$V_N(\zeta) = 4\pi\gamma[C_p C_t/(C_p + C_t)]b\Phi(\zeta), \tag{6}$$

where, $\Phi(\zeta)$ is the universal function,

$$\begin{aligned} \Phi(\zeta) &= -0.5(\zeta - 2.54)^2 - 0.0852(\zeta - 2.54)^3, \quad \zeta \leq 1.2511 \\ &= -3.437\exp(-\zeta/0.75), \quad \zeta \geq 1.2511 \end{aligned} \tag{7}$$

with surface separation ζ

$$\zeta = (r - C_t - C_p)/b, \tag{7a}$$

and central radius C

$$C = R(1 - b^2/R^2). \tag{7b}$$

[The small differences between $\Phi(\zeta)$ from Eq. (7) and the tabulated values in Ref. 6 are discussed in Appendix B.]

The imaginary absorptive potential is of the volume type, with Saxon-Woods form factor and depth W_0 (fixed at 10 MeV) and diffuseness a_I (fixed at 0.5 fm).

$$\begin{aligned} W_I(r) &= W_0\{1 + \exp[(r - R_I)/a_I]\}^{-1}, \\ R_I &= r_I(A_t^{1/3} + A_p^{1/3}). \end{aligned} \tag{8}$$

The radius parameter r_I is the only variable of the imaginary potential. In the optical model frictional effects are implicitly simulated by the imaginary potential.

The potential, $V_N(\zeta)$, Eq. (6) is a universal function of ζ, the distance between the nuclear surfaces measured in units of b. Therefore, an adjustment of Δb or ΔR causes a change of this distance scale in Eq. (7) and affects the magnitude of the potential in Eq. (6).[6] As the Coulomb potential is a function of the distance between the nuclear centers, these shifts or contractions of the parametrized surface distances alter the relative strength of Coulomb repulsion and nuclear attraction. Even very small changes in b and R lead to significant changes in the proximity force.[3,5,6]

The calculations we present have been made with the optical-model code A-3 of Auerbach.[14] Reference 3 shows the major qualitative effects for systematic variations of imaginary radius with all other parameters fixed. We have found that a rather large value of r_I can describe the boundary between elastic scattering and all reactions in the usual way. But in addition one can simulate the divisions between complete fusion and all other exit channels by a rather small value of r_I.[3] In this approach the dissipation of energy and angular momentum from relative to intrinsic motions is not explicitly addressed. This procedure differs from Ref. 10 where energy dissipation is directly addressed; at near-barrier energies large frictional effects are not expected. A more simple semiclassical calculation of the fusion cross section has also been made with the equation[3-5,12]

$$\sigma_{cf}(E) = \pi\lambda\!\!\!^{-2}\sum_{l=0}^{\infty}(2l+1)T_l(E). \tag{9}$$

The l-dependent real potential [nuclear plus Coulomb plus $l(l+1)\hbar^2/2\mu r^2$] is approximated near its maximum (energy E_{lm} and distance R_{lm}) by a parabola of curvature $\hbar\omega_{lm}$. Transmission coefficients $T_l(E)$ for each partial wave are then written

$$T_l(E) = \{1 + \exp[(2\pi/\hbar\omega_{lm})(E_{lm} - E)]\}^{-1}, \quad (10)$$

$$\hbar\omega_{lm} = \left| \frac{\hbar^2}{\mu} \frac{d^2V(r,l)}{dr^2} \right|^{1/2}_{R_{lm}}. \quad (11)$$

We will compare the results of these two methods in Appendix A. For the energy span explored in this paper for complete fusion (80–102 MeV) these methods are expected to be equivalent. We assume there is no low-l cutoff to fusion at these low energies.[13]

In the attempt to achieve a fit to the large body of data available,[15-18] we have proceeded as follows: (1) We alter the s-wave barrier maximum by changes in ΔR until we obtain a "best fit" to the complete fusion cross sections.[5] (2) We adjust the tail of the real potential (with fixed barrier maximum) by combined changes in Δb and ΔR until we obtain a "best fit" to σ/σ_{Ru} at $\theta_{1/4}(E)$.[3,4] (3) We adjust the imaginary potential via r_I and further refine Δb and ΔR (maintaining the fixed s-wave barrier) to get a "best fit" to the total reaction cross sections and to the detailed shapes of the elastic scattering cross sections.[3,4]

III. RESULTS OF THE CALCULATIONS

As a first step we present, in Fig. 1, a representation of calculations that result from the unaltered proximity potential (i.e., $\Delta b = \Delta R = 0$).[6] Firstly, as shown before, it is evident that the complete fusion cross sections are underestimated or that the s-wave barrier height is overestimated.[3-5,12] Secondly, if we select the value of r_I of 1.35 fm to fit the reaction cross sections,

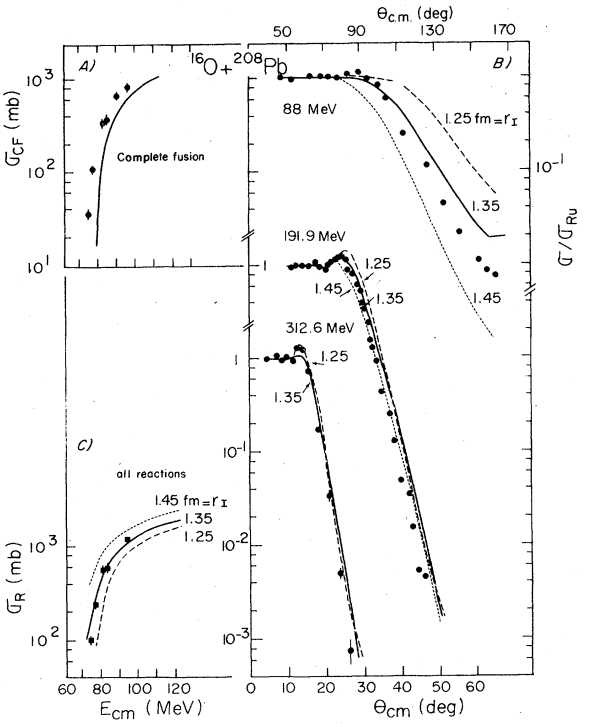

FIG. 1. Comparison of calculated (lines) and measured (points) cross sections for fusion σ_{cf}, all reactions σ_R, and elastic scattering σ/σ_{Ru} (laboratory energies are indicated). The recommended parametrization (Ref. 6) of the proximity potential has been used along with a Woods-Saxon imaginary potential with $W_0 = 10$ MeV, $a_I = 0.5$ fm, and r_I as indicated. For the calculation of σ_{cf}, see the text and Refs. 3, 5. Experimental data are from Refs. 15–18.

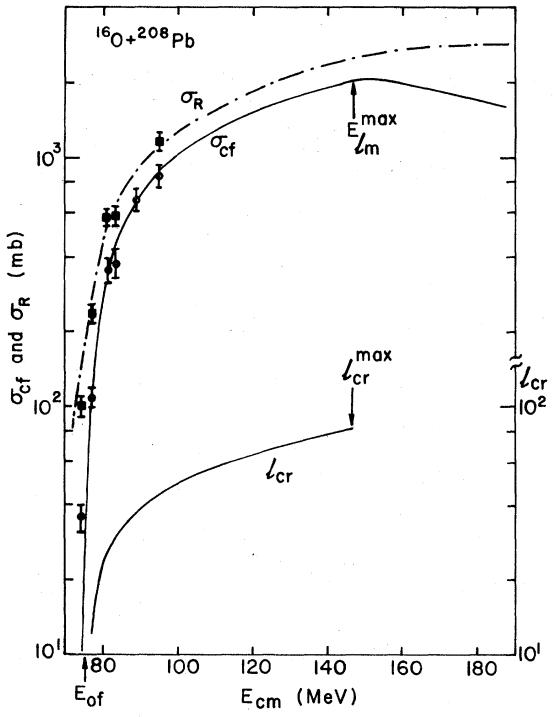

FIG. 2. Comparison of calculated and measured cross sections for fusion Eq. (9) and all reactions after parameter changes as described in the text ($\Delta b = -0.19$ fm, $\Delta R = 0.38$ fm, and $r_I = 1.33$ fm). For the quantum mechanical simulation of $\sigma_{cf}(E)$ see the Appendix A. For $E > E^{max}_{lm}$ σ_{cf} is calculated with the classical equation

$$\sigma_{cf}(E) = \pi\lambda^2(E)\,(l^{max}_{cr} + 1)^2.$$

The l value for classical orbiting (or l_{cr} in our model) is also indicated.

then the elastic scattering is overestimated at the larger angles at all energies. There is no single value of r_I that gives a satisfactory fit to the elastic scattering at higher energies. The overestimate of σ/σ_{Ru} suggests a need to strengthen the real potential. Such strengthening is also needed to lower the fusion barrier.[3,5]

Now we turn to parameter variations to try to achieve better fits. In Ref. 5 we found that $\Delta R = 0.23$ fm ($\Delta b = 0$) provided enough lowering of the real barrier to fit the fusion cross sections. In this work we applied the additional constraints of elastic and reaction cross sections via the sequence described above. In Figs. 2 and 3 we show the fits to σ_{cf}, σ_R and σ/σ_{Ru} that result for $\Delta b = -0.19$ fm, $\Delta R = 0.38$ fm, and $r_I = 1.33$ fm (note that $W_0 = 10$ MeV and $a_I = 0.5$ fm throughout). (A more detailed discussion of the sensitivity of the deduced potentials to measurable quantities is given in Appendix B.) We consider these fits to be satisfactory for σ_{cf} and σ_R for $E_{c.m.} \geq 80$ MeV and for σ/σ_{Ru} for $E_{lab} \geq 88$ MeV. Some details are not quite accounted for in these elastic scattering results, but it is probable that small experimental problems can explain them. It would appear that even after these adjustments systematic deviations for all three quantities result at the near barrier energies. (See also Refs. 5 and 19.) Our feeling is that the frozen sphere idealization is probably breaking down possibly because there is much more time available for dynamic deformations to occur during the long collision times for these near-barrier collisions.[20] Our major concern in this work is, however, not with these problems at near barrier energies. We will focus on the properties of the energy independent potential that gives such a good account for the large body of data at higher energies.

Now let us examine some of the features of the modified potential which has been obtained. In the lower part of Fig. 4 we show the modified and unmodified proximity potentials as a function of the distance between the nuclear centers. At fixed distance ($11 < r < 13$ fm) it is clear that the modification in $V_N(r)$ has been about a factor of 2. As

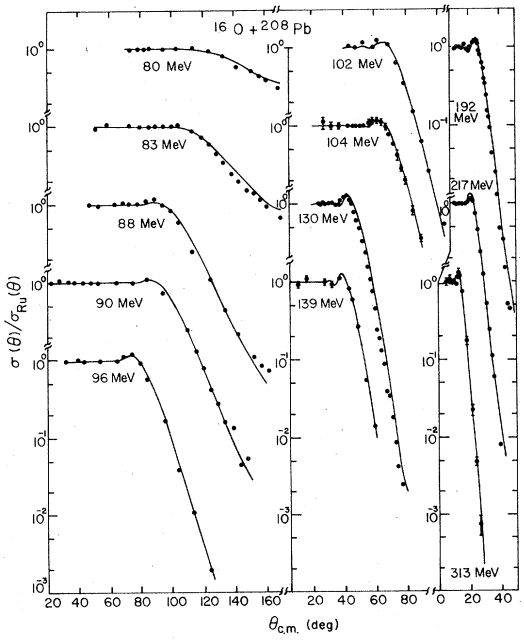

FIG. 3. Comparison of calculated and measured elastic scattering cross sections (ratio of measured to Rutherford scattering) at the various laboratory energies indicated (Refs. 15–18). Optical model calculations performed as described in the text with parameters indicated in the caption of Fig. 2.

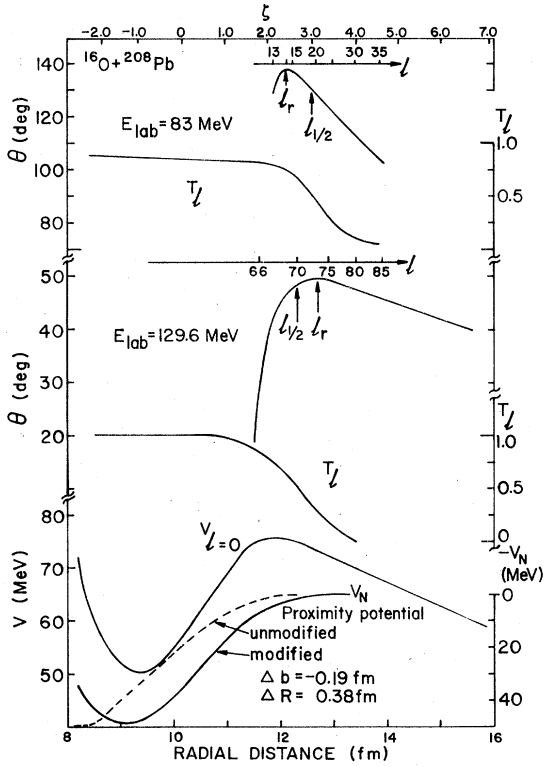

FIG. 4. Lower: The real nuclear potential for an unmodified proximity potential ($\Delta b = \Delta R = 0$) (lower scale only) and that modified to give the fits to data as shown in Figs. 2 and 3. The modified s-wave real potential (Coulomb plus nuclear) is also shown. Upper: Classical deflection functions (θ), as a function of the distance of closest approach between the nuclear centers (lower scale), the distance between nuclear surfaces (upper scale for the proximity force representation, ζ, and the corresponding l value as indicated. The value of l for half absorption ($T_l = \frac{1}{2}$), $l_{1/2}$, and for the classical rainbow l_r are shown.

discussed in Refs. 3, 5, and 12 we feel that such large changes in the net nuclear potential make it dangerous to assume that the frozen sphere idealization and/or the recommended parametrization of the proximity force[6] are satisfactory for quantitative calculations. However, if we assume that the basic features of the proximity force formulation are correct then we may search for an explanation for the discrepancy via two avenues: (1) deviations in the values of R and b for ^{16}O and/or ^{208}Pb from those of Eqs. (3) and (4),[21-25] or (2) the occurrence of dynamical shape or density changes.

Let us turn to the newer data from electron and proton scattering and mu mesic atoms to explore the first possibility.[26,27] The different radii we use in the framework of the proximity potential are effective radii in the sense that they result from the folding of two density distributions (proton and neutron). Each quantity (R or C) is then a combination of the distribution of protons (subscript Z) and of neutrons (subscript N) as, for example,

$$R=(NR_N+ZR_Z)/A\,. \tag{12}$$

One can also introduce the root-mean-square radius $\langle r^2\rangle^{1/2}$ and illustrate the consequences of the preceding statement

$$\langle r_Z{}^2\rangle^{1/2}=\left(\frac{3}{5}\right)^{1/2}R_Z\left(1+\frac{5}{2}\,\frac{b_Z{}^2}{R_Z{}^2}\right), \tag{13a}$$

$$\langle r^2{}_N\rangle^{1/2}=\left(\frac{3}{5}\right)^{1/2}R_N\left(1+\frac{5}{2}\,\frac{b_N{}^2}{R_N{}^2}\right), \tag{13b}$$

$$\langle r^2\rangle^{1/2}=\left(\frac{3}{5}\right)^{1/2}R\left(1+\frac{5}{2}\,\frac{b^2}{R^2}\right). \tag{13c}$$

Only a few of the variables used in these equations are determined experimentally; they are $C_Z, b_Z, \langle r_Z{}^2\rangle^{1/2}, \langle r_N{}^2\rangle^{1/2}$. Therefore, to deduce the effective quantities R, C, b needed here, theoretical models and experimental data become quite interwoven. Each aspect of this problem has been addressed by the droplet model. The formalism and the associated equations can be found in Refs. 22–25. The various coefficients that enter into calculation of the droplet model quantities have been recently re-evaluated with newer data on nuclear masses, fission barriers and radii.[24] The formula proposed by Blocki *et al.* for R [Eqs. (3) and (4)] is a polynomial fit to earlier values of R and b from the droplet model. This fit was made before the most recent coefficients were proposed. This could explain some of the small differences in R between Ref. 6 and the newer droplet model (Table I). Furthermore, the authors of Ref. 6 assumed a single value of b ($b = 1$ fm) for proton and neutron density distributions. This also leads to differences in the values of C obtained as compared to the droplet model. In Table I, the results obtained by these two models, are compared to the quantities deduced from our analysis for $^{16}O + ^{208}Pb$ and the independently measured experimental radii.[21-27] For ^{16}O we assume the measured charge radii are equal to the central neutron radii. In this case, if we take the experimental value of b for both distributions ($b_{exp} = 0.930$) we can get R via Eqs. (7b), (13a). For ^{208}Pb, we cannot deduce the effective values of R and C from the experimental data because we have no measurement of C_N. On the contrary, we can obtain the value of R effective [Eqs. (13a), (13b), (12)] from the experimental data and then deduce C using Eq. (7b) with effective values for R and b. We have estimated R and C with two different b values. In the first place, we have assumed the same experimental value of b for both distributions. In the second place, as in Ref. 25 we decrease the experimental value of b_Z by 9% to obtain b_N and b effective. This reduction is supposed to account for Coulomb effects on the charge density as described by Myers and Von Groote. In any event, the resulting effect on R and C is less than 1%.

This comparison is shown in Table I. First, we observe that the experimental values of b are very close to those from the droplet model but significantly different from our "best-fit value." Second, all the values of the root mean square radii are rather similar. However, the sum of the equivalent sharp radii R and central radii C obtained from our apparent "best fit values" are respectively about 0.7 and 0.8 fm larger than those obtained from the experimental values. The experimental values are, in turn, very close to those from the droplet model and from Eqs. (3) and (4). Therefore, the major aspect of the discrepancy seems not to be in the original parametrization of the values of R and b. Rather, the implication is that dynamic shape or density changes have occurred and the nuclear surfaces have reached out to try to touch one another. The larger values of C for projectile and target obtained in our analysis increase the nuclear potential by 18% due to the increase of the mean radius of curvature of the Gap function $\bar{C}=C_pC_t/(C_p+C_t)$. However, our reduction of the value of b (from 1.00 to 0.81) essentially cancels this effect [see Eq. (6)]. Thus the major effect of these parameter changes is the change in the surface distance ξ with respect to the distance between the charge centers.

If dynamic deformation is indeed occurring for these closed-shell nuclei, it has profound implications for the use of potential models for the analysis of many experiments. Presumably the potential energy should be formulated in more

TABLE I. Theoretical values of radii and surface widths in fm. (The values in parentheses are assumed values.)

	C_Z	b_Z	$\langle r_Z^2\rangle^{1/2}$	C_N	b_N	$\langle r_N^2\rangle^{1/2}$	R	C	b
					^{16}O				
Droplet model	2.529	0.886	2.717	2.542	0.854	2.674	2.805	2.535	0.870
Ref. 6	2.424	1.00	2.851	2.424	1.00	2.851	2.783	2.424	1.00
This work	2.956	0.81	2.852	2.956	0.81	2.852	3.163	2.956	0.81
				Independently measured values for ^{16}O					
Electron scattering[a]	2.608[c]	0.930[c]					2.906	2.608	0.930
		(0.930)	2.707[d]				2.691	2.370	(0.930)
Muonic atom[b]	2.4428[e]	(0.949)					2.768	2.443	(0.949)
			2.61		(0.930)		2.507	2.162	(0.930)
			2.71		(0.930)		2.697	2.376	(0.930)
					^{208}Pb				
Droplet model	6.570	1.00	5.49	7.006	0.91	5.742	6.963	6.829	0.966
Ref. 6	6.626	1.00	5.533	6.938	1.00	5.757	6.959	6.774	1.00
This work	7.062	0.810	5.719	7.371	0.810	5.948	7.339	7.250	0.810
				Independently measured values for ^{208}Pb					
Electron scattering[a]	6.624[g]	0.873[g]	5.502[h]						
Proton scattering[f]		(0.873)	5.443		(0.873)	5.625	6.893[i]	6.782	(0.873)
					(0.794)	5.625	6.922[j]	6.821	(0.838)
Muonic atom[b]	6.712	0.873	5.4978						

[a] Data from Ref. 26, p. 489 for ^{16}O and p. 494 for ^{208}Pb.
[b] Data from Ref. 26, p. 522 and 551 for ^{16}O and p. 548 and 581 for ^{208}Pb.
[c] Results obtained with a three-parameter Fermi distribution.
[d] Average value. The standard deviation is 0.029 fm.
[e] Result from a fit to the data assuming a two-parameter Fermi distribution with "best fit value" of $b = 0.949$ fm. See Ref. 26.
[f] Data from Ref. 27.
[g] Results obtained with a two-parameter Fermi distribution.
[h] Average value. The standard deviation is 0.012 fm.
[i] The deduced neutron skin thickness is 0.25 fm compared to 0.31 fm from Ref. 6 and 0.40 fm from the droplet model.
[j] In this case, the neutron skin thickness is 0.29 fm. See footnote i.

complex terms than simply the distance between the centers of mass. One such possibility would be to reformulate the proximity potential so as to allow dynamical adjustments of the surface width b as the two nuclei approach. Such a reformulation clearly steps outside the frozen sphere idealization and would probably call for a completely different potential parametrization from that we have deduced. (In particular the negative value of Δb runs contrary to physical intuition.) Our major point in this paper is simply that dynamic shape or density adjustments seem to be called for. If this conclusion stands the test of time, it will have far-reaching implications for the use of potential models in heavy ion reactions. Therefore, we are confident that this result will be looked at from many angles before such complex formulations of the potential energy are attempted. In the meanwhile, one might take the position that the frozen-sphere potential parametrization presented here is interesting in its own right. It is energy independent and accounts for a larger data base than, for example, the energy dependent parametrizations of Ref. 17. In this context it is interesting to look at its properties as in Refs. 3, 4, 15, 28, and 29.

One of the most important aspects of any conservative potential representation is the relative strength of absorption and refraction in the nuclear surface. For the proximity potential as modified

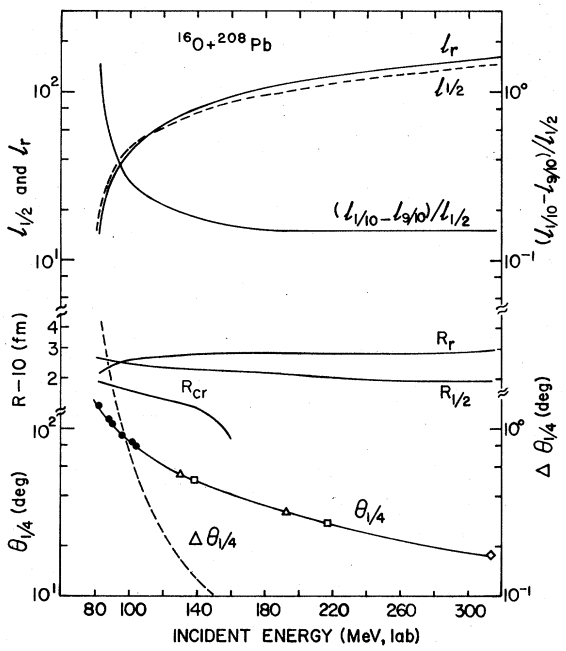

FIG. 5. Lower: Calculated (line) and measured values for the elastic quarter points $\theta_{1/4}$ (points) (●, Ref. 16; △, Ref. 15; □, Refs. 17, 18). The $\Delta\theta_{1/4}$ values are differences between $\theta_{1/4}$ values calculated with the optical model with $r_I=1.27$ fm, and $r_I=1.33$, and proximity potential parameters of Fig. 2. Upper: Calculated values of l and classical approach distance R for half absorption (subscript $\frac{1}{2}$) and rainbow (subscript r). The critical distances for complete fusion R_{cr} are explained in the text. To expand the radius scale we plot R-10 fm. The width of the smooth cutoff in T_l values, calculated with the optical model (see caption of Fig. 2) is given by $(l_{1/10}-l_{9/10})/l_{1/2}$, where the subscript indicates the value of T_l.

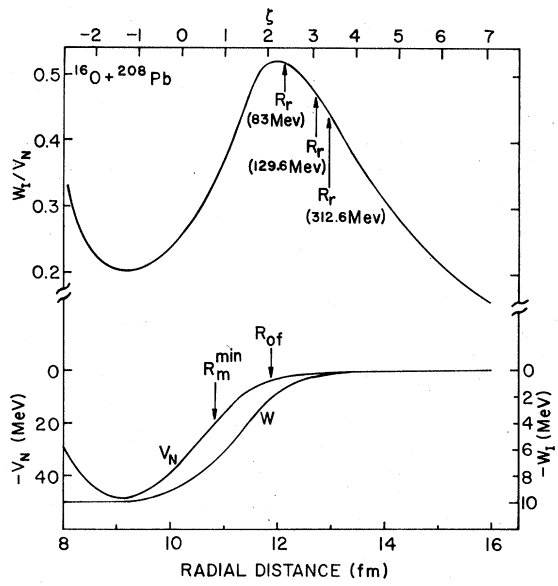

FIG. 6. Lower: Modified real and imaginary potentials (for parameters, see Figs. 2 and 3) on two scales as also shown in Fig. 4. The range of fusion radii is also indicated by the arrows. ($R_{of}=R_{cr}$ for $l=0$; $R_m^{min}=R_{cr}$ for l_{cr}^{max} as in Ref. 5.) Upper: The ratio of imaginary to real potentials W_I/V_N on the same two scales; same potential parameters as in the lower part. The range of rainbow radii is also indicated by the arrows.

here we show some of these features in terms of classical deflection angles and distances of approach and quantum mechanical transmission coefficients for the corresponding partial waves. In the upper parts of Fig. 4 the deflection functions are shown on three scales for two incident energies.[30] Both curves have the same scales of radial distance and surface separation for the closest approach of each classical trajectory (characterized by an impact parameter or orbital angular momentum $l\hbar$). The separate scales for l at each energy are also indicated. The transmission coefficients obtained from the optical model calculations are also shown on the same scales. Arrows indicate the l values of the classical rainbow (l_r)[3,4] and those for $T_l=\frac{1}{2}$ $(l_{1/2})$. We see that at low energy (83 MeV) $l_{1/2}>l_r$ and the reverse at high energy (129.6 MeV). This suggests that the absorptive part of the potential is cutting off the elastic scattering at low energies while the refractive part is dominating at high energies.[4,5] More details are given in the Appendices.

This feature is explored further in Figs. 5 and 6. In the lower part of Fig. 5 we show measured and calculated values of $\theta_{1/4}$ from the elastic scattering. The dashed curve for $\Delta\theta_{1/4}$ shows the differences between calculated values of $\theta_{1/4}$ for $r_I=1.27$ and $r_I=1.33$ fm. These values of $\Delta\theta_{1/4}$ decrease very rapidly with increasing energy reflecting a diminishing sensitivity of $\theta_{1/4}$ to the imaginary potential. In Refs. 3 and 4 we showed that calculated values of $\theta_{1/4}$ retain their sensitivity to the real potential at high energies. In terms of the classical trajectories this might be said to be related to the relative magnitudes of l_r and $l_{1/2}$ (upper Fig. 5) or R_r and $R_{1/2}$ (mid Fig. 5).

The curves for l_r and $l_{1/2}$ cross at ≈90 MeV with refraction becoming dominant for higher energies (see also the Appendices). The associated distances of closest approach R_r and $R_{1/2}$ have, of course, the same trend but it is also interesting to compare them to the critical distances R_{cr} for complete fusion. The values of R_{cr} decrease with increasing energy and are less than $R_{1/2}$ by 1 fm or more. These quantities (R_{cr}) refer to the maxima in the l-dependent potentials for the value of l_{cr} at each energy.[3-5]

$$E = V(R_{cr}, l_{cr}),$$
$$\left.\frac{dV(r,l)}{dr}\right|_{R_{cr},l_{cr}} = 0. \quad (14)$$

In this model there is no fusion for $l > l_{cr}^{max}$ as those values of l have no pocket in the real potential. Thus for higher energies R_{cr} is constant at the value R_m^{min}.

Figure 6 shows the radial and ζ dependences of the real and imaginary potentials and their ratio. Arrows indicate the span of the rainbow radii[3,4] and the fusion radii and thus give some feeling for the zone of exploration of each type of measurement. For the most important range for the elastic scattering W_I/V_N is 0.5 to 0.4; these values are somewhat larger than we indicated before[4] and smaller than those given in Refs. 15 and 29.

IV. CONCLUSIONS

We have used the form of the proximity potential in an attempt to account for many experimental studies of the reaction system $^{16}O + ^{208}Pb$. With three free parameters b and R (proximity potential) and r_I (imaginary potential) we can describe most of the features of complete fusion, reaction, and elastic scattering cross sections. The modified proximity potential that emerges is very strong, and surface refraction dominates the elastic scattering except for energies near to the barrier ($\lesssim$90 MeV, lab). The best-fit values of the modified parameters R and b differ significantly from independently measured values. If the proximity force formulation is correct, then dynamic shape or density changes are implied, and the nuclear surfaces seemingly reach out toward one another.

ACKNOWLEDGMENTS

Very helpful comments have been made by W. Swiatecki, W. D. Myers, and J. Randrup concerning the proximity potential, the frozen sphere approximation and the droplet model and by C. Marty concerning deflection functions. We thank E. H. Auerbach and M. Gai for assistance with the A-3 program on the Stony Brook computer. We appreciate the data tables sent to us by the authors of Refs. 15–18. Hospitality at Stony Brook is appreciated by H. Delagrange and L. C. Vaz.

This work was supported in part by FINEP of Brazil, CNRS of France, and the United States Department of Energy.

APPENDIX A: SOME PROPERTIES OF THE S MATRIX, VARIOUS l VALUES, AND SEVERAL WAYS TO CALCULATE FUSION CROSS SECTIONS

It has been shown in Refs. 3 and 4 that for the system $^{16}O + ^{208}Pb$ at energies $\lesssim$90 MeV, the Coulomb rainbow distance R_r is less than the strong absorption distance $R_{1/2}$. By contrast, for energies >90 MeV, the Coulomb rainbow radius R_r is greater than the strong absorption radius $R_{1/2}$. These effects are clearly highlighted in Table II and Fig. 7, where we have plotted the reflection coefficient, $|S_l|$, versus the partial wave l.[28] The S matrix is calculated with the optical model with the same potential parameters as in Fig. 2. In

TABLE II. The various important angular momenta, classical distances, and complete fusion cross sections.

E (MeV)	$l_{1/2}$	l_r	l_m	l_{cr}	$R_{1/2}$ (fm)	R_r (fm)	R_{cr} (fm)	Fusion cross sections (mb) σ_{exp}[a]	σ_{SC}[b]	σ_Q[c]
80	8.7		12					36±4	12	17
83	19.2	13.9	17	13	12.58	12.09	11.86	108±10	104	113
88	29.3	27.4	26	25.1	12.52	12.30	11.79	350±40	342	350
90	32.5	31.2	29	28.5	12.50	12.34	11.76	377±50	431	440
96	40.5	40.7	37	36.9	12.45	12.47	11.69		674	686
102	47.2	48.1	44	43.6	12.41	12.53	11.62	844±90	885	900
104	49.2	50.2	46	45.6	12.40	12.53	11.60		949	965
129.6	69.9	73.5	66	65.6	12.28	12.71	11.38		1581	1601
138.5	75.7	80.1	72	71.1	12.25	12.75	11.32		1739	1759
191.9	103.7	112.1	98		12.11	12.84			1714	
216.6	114.1	122.6	108		12.06	12.84			1519	
312.6	147.5	161.1	140		11.94	12.94			1052	

[a] Experiment Ref. 16.

[b] Semiclassical calculations with real potential as in Fig. 2 (Refs. 3,5).

[c] Optical-model simulation with the same real potential as in Fig. 2, but with $W_0 = 10$ MeV; $a_I = 0.5$ fm and $r_I = 1.12$ fm.

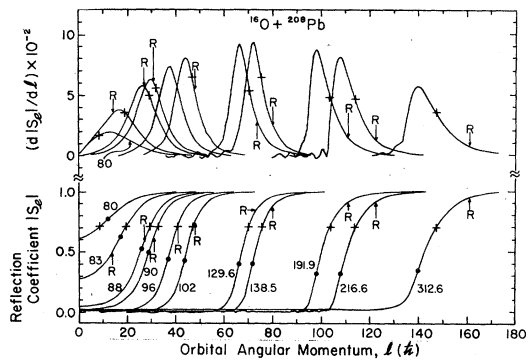

FIG. 7. Lower: reflection coefficient, $|S_l|$ vs l. The symbol + indicates $l_{1/2}$ ($T_{l_{1/2}}=\frac{1}{2}$, optical model), the symbol R indicates l_r [classical calculation with only the real potential (Ref. 3)] and ● indicates the point of inflection in $|S_l|$. Each curve is labeled by the laboratory energy. Upper: Shape absorptive function vs l. Notice the maximum which gives l_m for each energy. The optical potential used in these calculations is that used for Fig. 2.

Fig. 7 we have labeled $l_{1/2}$ ($T_{l_{1/2}}=\frac{1}{2}$, optical model) with a cross; l_r (corresponding to the classical rainbow) is labeled R with an arrow; l_m (corresponding to the maximum in the shape absorptive function $d|S_l|/dl$, from Fig. 7 upper) is indicated by the solid point. We make the following observations from Fig. 7.

(i) For energies $\leq$90 MeV, $l_r < l_{1/2}$ (i.e., l for the Coulomb rainbow (l_r) is less than that for strong absorption $l_{1/2}$). Also $l_r > l_{1/2}$ for all energies >96 MeV. Their difference $(l_r - l_{1/2})$ increases with increasing bombarding energy. We also note that the absorption $(1 - |S_l|^2)$ at l_r continuously decreases with energy.

(ii) For all energies above 83 MeV (i.e., above the s-wave fusion barrier), $l_m < l_{1/2}$. At energies slightly above the fusion barrier (i.e., $E_{0f} \lesssim E < 88$ MeV) l_r is even less than l_m. Hence from the curves in Fig. 7 we observe that the absorption at the classical rainbow l_r is predicted to be even greater than that at the strong absorption point, $l_{1/2}$. Therefore, as demonstrated in Refs. 3 and 4, this analysis emphasizes that surface absorption dominates the elastic scattering at near-barrier energies and the reverse at much higher energies (>90 MeV).

(iii) Except for energies very close to the barrier, l_m (which corresponds to the point of inflection of the reflection function (i.e., a maximum in the shape absorptive function) is almost equal to l_{cr} [given by the classical orbiting condition, Eq. (14)]. For fusing collisions [Eq. (10)] the transmission of the critical partial wave is one half, whereas the total transmission coefficient of the partial wave l_m calculated by the optical model is always greater than one half. Also it increases with energy (from 0.4 at 83 MeV to above 0.9 at 313 MeV). The identification of l_m as a strong absorption l for all reactions[28] would not seem to be appropriate for this potential. However, possibly by accident, l_m seems to be essentially equal to l_{cr} for energies $\gtrsim$88 MeV.

It has been shown in Ref. 3 that the fusion cross sections can be simulated by an optical potential with an imaginary radius, R_I, much less than that needed for the description of total-reaction and elastic scattering cross sections. Complete fusion cross sections calculated with this method[3] are compared with the semiclassical model [Eqs. (9)–(11)] in Table II. The results are very similar for this energy range, and therefore we consider them essentially equivalent (except, of course, for energies well below the barrier).

APPENDIX B: SOME ASPECTS OF THE SENSITIVITY OF THE DEDUCED POTENTIALS TO MEASURABLE QUANTITIES

The first step of the sequence we follow is the adjustment of the real potential barrier to that required to fit the complete fusion cross sections (see Figs. 1 and 2). Then we vary the shape of the real potential by combined changes in Δb and ΔR of the proximity formulation. We show in Fig. 8 a family of modified proximity potentials that are constrained to the same barrier height. We then turn to the elastic scattering and reaction cross sections to try to select among this family of real potentials. For this selection we assume that neither real nor imaginary potential changes significantly with energy. This is a very demanding constraint and makes it very difficult to obtain completely satisfying fits.

What now is the nature of the constraints imposed by scattering and reaction cross sections, and to what extent are there ambiguities between the real and the imaginary potentials? As we have only allowed variations in Δb, ΔR, and r_I there is not a large range of possibilities, and we have not searched in detail for alternatives. We have sought reasonable fits for each angular distribution over the whole range of energies. Nevertheless, from curves such as those in Figs. 8 and 9 we are convinced that a major change in the deduced real potential ($11.8 < r < 13$ fm) would require a major change in the assumptions. In Figs. 8 and 9 (upper) we show that the values of $\theta_{1/4}$ as well as the whole descent of σ/σ_{Ru} are sensitive to the real potential. Fig. 9 (lower) shows that at high energies the major sensitivity to the imaginary potential is in the region near the maximum in σ/σ_{Ru} and at very large angles. Figure 1 shows the special sensitivity to $W(r)$ for both elastic and reaction cross sections at near barrier energies.

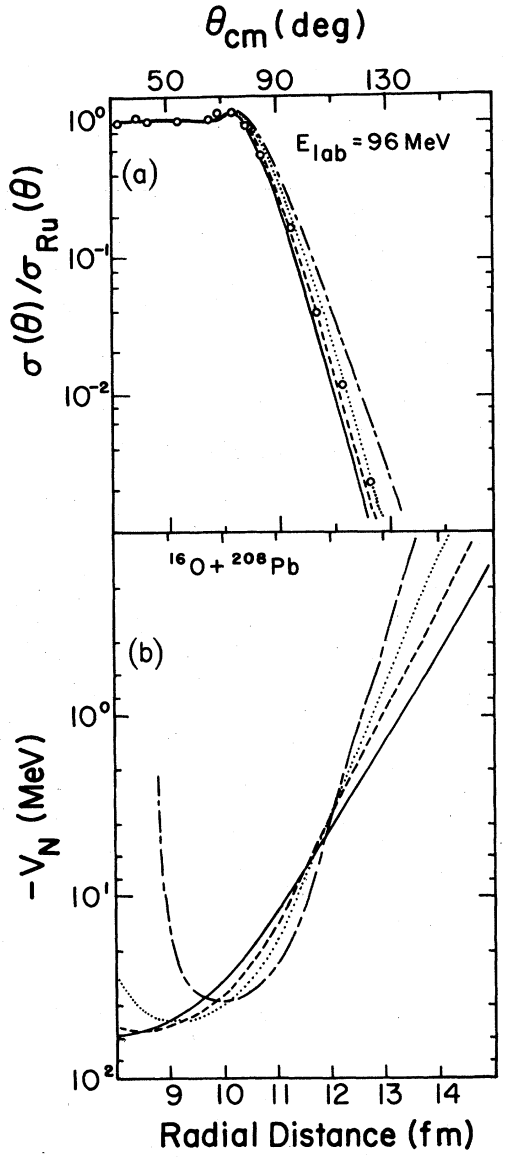

FIG. 8. (a) Comparison of calculated and measured elastic scattering cross sections at 96 MeV. The different curves are for the different real potentials as shown below. In each case $r_I = 1.33$ fm. (b) Family of real potentials that conserve the same fusion barrier. Symbols are as follows for the proximity potential parameters Δb and ΔR in fm: ——— $\Delta b = 0.2$, $\Delta R = 0.11$; – – – $\Delta b = 0$, $\Delta R = 0.23$; ..... $\Delta b = -0.19$, $\Delta R = 0.38$; —·—·— $\Delta b = -0.4$, $\Delta R = 0.59$.

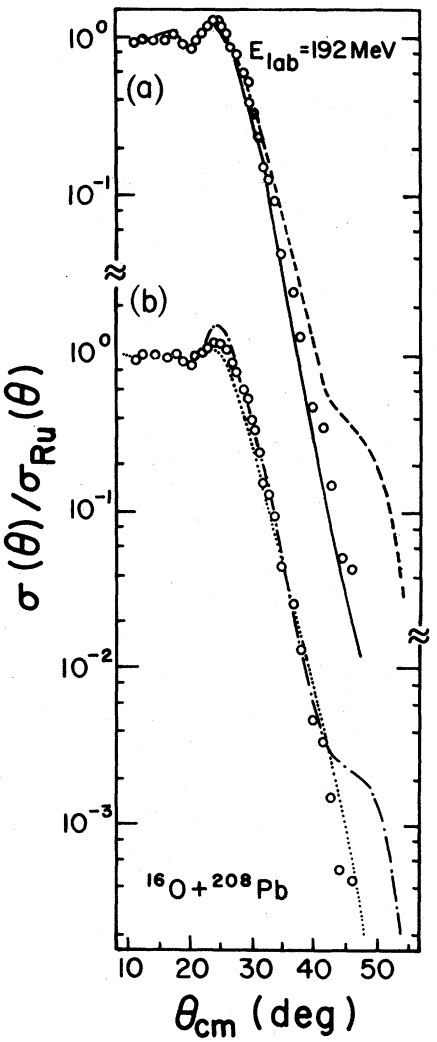

FIG. 9. Comparison of calculated and measured elastic scattering cross sections at 191.9 MeV. (a) For different real potentials: ——— $\Delta b = 0.2$ fm, $\Delta R = 0.11$ fm; – – – $\Delta b = -0.4$ fm, $\Delta R = 0.59$ fm. In each case $r_I = 1.33$ fm. (b) For different imaginary potentials: ····· $r_I = 1.43$ fm; —·— · $r_I = 1.23$ fm. In each case $\Delta b = -0.19$ fm, $\Delta R = 0.38$ fm.

From these features of the fits we feel that the real potential at large r is heavily constrained by $\theta_{1/4}$ and σ/σ_{Ru} for the higher energies. Likewise, we feel that the imaginary potential is constrained at near barrier energies. If one allows a strong energy dependence of the potential then, of course, our conclusions would have to be reassessed. Similarly, if the potential that governs fusion is very different from that which controls elastic scattering then the conclusions could be changed.[29] We find it very interesting that it is possible to account for such a wide range of data with a single parametrization.

In this whole development we have used the analytic formulas [Eq. (7)] to represent the universal proximity function $\Phi(\zeta)$.[6] The possibility of significant change between the analytic and the tabulated numerical values of $\Phi(\zeta)$ has also been explored.

TABLE III. Values of ΔR and Δb that lead to equivalent nuclear potentials from the analytic and the tabulated proximity functions $\Phi(\xi)$.

Analytic $\Phi(\xi)$ [a]				Tabulated $\Phi(\xi)$ [b]			
ΔR (fm)	Δb (fm)	E_{of} (MeV)	R_{of} (fm)	ΔR (fm)	Δb (fm)	E_{of} (MeV)	R_{of} (fm)
0.0 [c]	0.0	79.25	11.09	−0.03	0.0	79.11	11.12
0.23 [c]	0.0	75.25	11.73	0.20	0.0	75.16	11.76
0.38	−0.19	75.27	11.90	0.33 [d]	−0.17	75.21	11.90
0.11	0.20	75.27	11.56	0.05	0.25	75.28	11.52
0.59	−0.40	75.26	12.06	0.57	−0.40	75.17	12.08

[a] These nuclear potentials $V_N(r)$ are shown in Figs. 4 or 8.

[b] For each potential $V_N(r)$ calculated from Eqs. (3)–(7) we made a least squares fit of $V_N(r)$ calculated from tabulated values of $\Phi(\xi)$ (Ref. 6). The resulting values of ΔR, Δb, E_{of}, and R_{of} are shown. The root-mean-square difference between fitting and fitted functions $V_N(r)$ is $\approx 2\%$.

[c] Least squares fit for these cases made between 11.0 and 12.5 fm as we are only interested in the fusion barrier. Only ΔR was varied here.

[d] This potential leads to calculated values of σ/σ_{Ru} that are essentially the same as those shown in Fig. 3. The values of $\sigma_{cf}(E)$ at low energies are also very similar to the calculated curve in Fig. 2, except that $E_{lm}^{\max}$ occurs at 122 MeV (c.m.).

We have made least-squares fits ($11.3 < r < 13$ fm) of $V_N(r)$ calculated from the tables of $\Phi(\xi)$ to those analytic functions for $V_N(r)$ shown in Fig. 8. In Table III we show the values of ΔR and Δb required to give essentially the same nuclear potentials. For the region of ξ relevant to this study, the tabulated values of $\Phi(\xi)$ give a somewhat stronger nuclear potential than the analytic functions [Eq. (7)]. Therefore, the values of ΔR and Δb needed to achieve a given real potential are somewhat smaller. As shown in Table III, these values of ΔR and Δb are very similar; therefore the arguments presented do not depend substantially on this detail for $\Phi(\xi)$.

*Permanent address: Centre d'Etudes Nucleaires de Bordeaux-Gradignan, 33170 Gradignan, France.

[1] L. C. Vaz and J. M. Alexander, Phys. Rev. C 10, 464 (1974); J. M. Alexander, L. C. Vaz, and S. Y. Lin, Phys. Rev. Lett. 33, 1487 (1974).

[2] J. M. Alexander, H. Delagrange, and A. Fleury, Phys. Rev. C 12, 149 (1975).

[3] L. C. Vaz, J. M. Alexander, and E. H. Auerbach, Phys. Rev. C 18, 820 (1978).

[4] L. C. Vaz and J. M. Alexander, Phys. Rev. C 18, 833 (1978).

[5] L. C. Vaz and J. M. Alexander, Phys. Rev. C 18, 2152 (1978).

[6] J. Blocki, J. Randrup, W. J. Swiatecki, and C. F. Tsang, Ann. Phys. (N.Y.) 105, 427 (1977).

[7] See W. U. Schröder and J. R. Huizenga, Annu. Rev. Nucl. Sci. 27, 465 (1977).

[8] J. R. Birkelund and J. R. Huizenga, in Proceedings of the Symposium on Heavy-Ion Elastic Scattering, Rochester, N.Y., 1977 (unpublished).

[9] J. R. Birkelund and J. R. Huizenga, Phys. Rev. C 17, 126 (1978).

[10] J. R. Birkelund, J. R. Huizenga, J. N. De, and D. Sperber, Phys. Rev. Lett. 40, 1123 (1978).

[11] S. L. Tabor, D. A. Goldberg, and J. R. Huizenga, Phys. Rev. Lett. 41, 1285 (1978).

[12] K. Siwek-Wilczyńska and J. Wilczyński, Phys. Lett. 74B, 313 (1978).

[13] P. Bonche, B. Grammaticos, and S. Koonin, Phys. Rev. C 17, 1700 (1978); S. J. Krieger and K. T. R. Davies, *ibid* 18, 2567 (1978).

[14] E. H. Auerbach, Comput. Phys. Commun. 15, 165 (1978).

[15] J. B. Ball, C. B. Fulmer, E. E. Gross, M. L. Halbert, D. C. Hensley, C. A. Ludemann, M. I. Saltmarsh, and G. R. Satchler, Nucl. Phys. A252, 208 (1975).

[16] F. Videbaek, R. B. Goldstein, L. Grodzins, S. G. Steadman, T. A. Belote, and J. D. Garrett, Phys. Rev. C 15, 954 (1977).

[17] S. C. Pieper, M. H. Macfarlane, D. H. Gloeckner, D. G. Kovar, F. D. Becchetti, B. G. Harvey, D. L. Hendrie, H. Homeyer, J. Mahoney, F. Pühlhofer, W. von Oertzen, and M. S. Zisman, Phys. Rev. C 18, 180 (1978).

[18] C. Olmer, M. Mermaz, M. Buenerd, C. K. Gelbke, D. L. Hendrie, J. Mahoney, D. K. Scott, M. H. Macfarlane, and S. C. Pieper, Phys. Rev. C 18, 205 (1978).

[19] H. Delagrange, L. C. Vaz, and J. M. Alexander. Several types of systems have been also investigated with the optical model along similar lines. Results to be published.

[20] H. Holm, W. Scheid, and W. Greiner, Phys. Lett. B29, 473 (1969).

[21] H. R. Collard, L. R. B. Elton, and R. Hofstadter, in

Nuclear Radii, *Vol*. 2, Group I Landolt-Bornstein, Numerical Data and Functional Relationships in Science and Technology (Springer, Berlin, 1967).
[22]W. D. Myers, Nucl. Phys. A204, 465 (1973).
[23]W. D. Myers, Phys. Lett. 30B, 451 (1969).
[24]W. D. Myers, At. Data Nucl. Data Tables 17, 411 (1976).
[25]W. D. Myers and H. von Groote, Phys. Lett. 61B, 125 (1976).
[26]C. W. De Jager, H. De Vries, and C. De Vries, At. Data Nucl. Tables 14, 479 (1974); R. Engfer, H. Schneuwly, T. L. Vuilleumier, H. K. Walter, and A. Zehnder, *ibid*. 14, 509 (1974).
[27]L. Ray, W. R. Coker, and G. W. Hoffman, Phys. Rev. C 18, 2641 (1978).
[28]W. E. Frahn and D. H. E. Gross, Ann. Phys. (N.Y.) 101, 520 (1976); W. E. Frahn, Nucl. Phys. A302, 281 (1978).
[29]G. R. Satchler and W. G. Love, Phys. Rep. C (to be published).
[30]Deflection functions have also been obtained from the optical model phase shifts ($\theta = 2 d\eta_l/dl$) from the A-3 code with integer l values. These functions approach the classical curves for the larger l values but exhibit oscillations for smaller l values. Nevertheless, for energies $\geq$ 129.6 MeV rainbow angles are apparent with essentially the same values as those obtained classically. Quantum mechanical deflection functions can also be obtained without the limitation of the integral values of l as described by S. Y. Lee, N. Takigawa, and C. Marty, Nucl. Phys. A308, 161 (1978). We plan to make these calculations but we expect no significant changes in the rainbow properties for energies $\geq$ 129.6 MeV.